

Design and analysis of a low-threshold polymer circular-grating distributed-feedback laser

Guy F. Barlow and Alan Shore

School of Informatics, University of Wales, Bangor, Gwynedd, Wales LL574TA, UK

Graham A. Turnbull and Ifor D. W. Samuel

School of Physics and Astronomy, University of St. Andrews, Fife, KY16 9SS, UK

Received March 3, 2004; revised manuscript received July 23, 2004; accepted August 6, 2004

A transfer-matrix technique is used to calculate the lasing thresholds of second-order circular-grating polymer lasers operating at 630 nm. By use of poly[2-methoxy-5-(2'-ethyl-hexyloxy)-*p*-phenylenevinylene] as an example polymer material, it is also shown how known optical properties of polymeric materials may be incorporated into the analysis of both the transverse waveguiding and the distributed feedback in circular-grating distributed-feedback polymer lasers. © 2004 Optical Society of America

OCIS codes: 140.0140, 140.3410.

1. INTRODUCTION

As active materials in optoelectronic devices, semiconducting polymers offer advantages in terms of mechanical flexibility and low-cost fabrication. High photoluminescence yields and wide emission spectra have been observed in certain polymers for some time, and efforts to design working lasers with polymers and other organic materials continue. Although considerable success has been achieved with optically excited organic distributed-feedback (DFB) lasers,^{1,2} lasing in an electrically pumped amorphous polymer laser has yet to be demonstrated. The main obstacle to designing electrically operated polymer lasers is the high degree of induced absorption at charge densities associated with lasing.

Experimentally, it has been found that charge-induced absorption varies greatly between polymers. The identification of polymers well suited to being electrically pumped is a continuing challenge. In working toward that aim, it is of interest to use the unique mechanical and optical properties of polymer materials to design microstructures to reduce other losses in the device as much as possible.

Soft lithographic techniques, such as contact imprinting,³ are being developed as low-cost fabrication methods for organic lasers. Imprinting permits essentially any microstructured relief pattern to be easily applied at a material interface in the transverse structure. With this technique, a grating of almost any shape may be designed to confine or couple light in or out of the device. In particular, it has been suggested that circular-grating DFB (CG-DFB) lasers are of considerable interest as imprinted polymer laser designs. CG-DFB laser designs potentially offer advantages in term of low-threshold operation and vertical emission out of the device plane. In addition to the simplicity of the structures, these features make CG-DFB lasers an attractive design for organic vertical-cavity surface-emitting arrays.

This paper investigates the design of CG-DFB lasers by use of the well-characterized poly[2-methoxy-5-(2'-ethyl-hexyloxy)-*p*-phenylenevinylene] (MEH-PPV) polymer as an active material. A typical CG-DFB design is shown in Fig. 1. It is composed of a grating of concentric circular grooves on a film of polymer material that forms the active layer. The grating shown in the figure is located at the air-polymer interface, where it may be formed by an imprinting process following the deposition of the polymer.

The current paper forms the theoretical component of a collaboration between groups at the University of Wales, Bangor, and The University of St. Andrews. Experimental research relating to the characterization of the polymer materials as well as experimental data on completed polymer CG-DFB lasers is to be published concurrently.

2. OPTICAL PROPERTIES OF POLYMERS

As a typical semiconducting photoluminescent polymer, MEH-PPV has wide emission and absorption spectra. Furthermore, the transfer of energy between absorptive and emissive sites leads to a large gap between absorption and emission peaks. For this reason, losses through reabsorption in polymer lasers can normally be assumed to be negligible.

Experimental research performed at St. Andrews has shown that MEH-PPV exhibits strong absorption around typical pump wavelengths of 440 and 500 nm. The pump energy, and thus the density of excitation, will therefore attenuate sharply with distance from whichever surface the pump is being applied. This is an important factor in selecting the optimum thickness for the film.

3. ANALYSIS TECHNIQUES

A. Optimization of Transverse Waveguide Characteristics

The TE and TM modes in the MEH-PPV film waveguide are analyzed with a semianalytical technique,⁴ in which

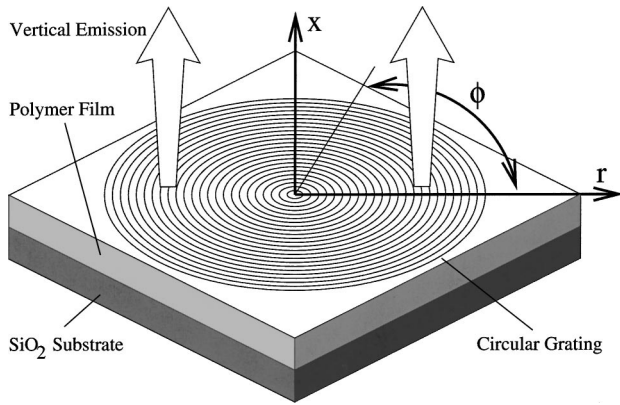


Fig. 1. General CG-DFB design.

the Helmholtz wave equation is solved subject to appropriate boundary conditions at the layer interfaces. With $n_o(\lambda)$ as the wavelength-dependent refractive index, where λ is the wavelength in nanometers, the dispersion of the polymer is represented with a Sellmeyer formula [Eq. (1)] fitted to experimental data:

$$n_o(\lambda) = \left[3.3 + \frac{0.148}{1 - (552/\lambda)^2} - 9.7 \times 10^{-7} \lambda^2 \right]^{1/2}. \quad (1)$$

It is normally convenient to use a confinement factor that relates the gain carried by the mode to the total gain available. Using the system of cylindrical coordinates shown in Fig. 1 and assuming the field is separable into transverse and lateral components, one can write the inhomogeneous Helmholtz equation for the planar structure as

$$\frac{\partial^2}{\partial x^2} E(x) + [n^2(x) - n_{\text{eff}}^2] k_o^2 E(x) = 0, \quad (2)$$

where $E(x)$ is the field amplitude profile, n is the x -dependent refractive index, k_o is the wave number of free space (given by $2\pi/\lambda$), and n_{eff} is an effective refractive index for the structure. In general, n and n_{eff} are complex parameters, with imaginary parts corresponding to gain or absorption as follows:

$$n(x) = n_o(x) - j \frac{\alpha_o(x)}{2k_o}, \quad (3)$$

$$n_{\text{eff}} = n_e - j \frac{\alpha_e}{2k_o}, \quad (4)$$

where α_o and α_e are the local and effective gain-loss coefficients, respectively. Terms involving the square of the loss coefficients may be ignored in most practical cases. Substitution of Eqs. (3) and (4) into Eq. (2) then gives

$$\frac{\partial^2}{\partial x^2} E(x) + [n_o^2(x) - n_e^2] k_o^2 E(x) - j [n_o(x) \alpha_o(x) - n_e \alpha_e] k_o E(x) = 0. \quad (5)$$

In a passive waveguide (one having no gain or loss), the first three terms of Eq. (5) would form the wave equation for the structure. Gain guiding is not expected to be a

strong mechanism, and so the solutions in terms of $E(x)$ will be identical to those for a passive waveguide. Hence the perturbation for the passive waveguide satisfies

$$n_e \alpha_e E(x) = n_o(x) \alpha_o(x) E(x). \quad (6)$$

Outside the polymer, the gain is assumed to be zero. The gain profile throughout the polymer is

$$\alpha_o(x) = \alpha_s \exp(-\alpha_p x), \quad 0 < x < d, \quad (7)$$

where α_s is the level of gain at the air-polymer interface, α_p is the absorption of MEH-PPV at the pump wavelength of 550 nm, and d is the layer thickness. One may then remove the x dependence of Eq. (6) by multiplying throughout by $E(x)$ and integrating both sides with respect to x . A confinement factor for the mode is thus obtained, relating the ratio of the effective and surface loss coefficients:

$$\alpha_e = \alpha_s \Gamma_e, \quad (8)$$

with

$$\Gamma_e = \frac{\int_{x=0}^d E^2(x) \exp(-2\alpha_p x) dx}{\int_{-\infty}^{\infty} E^2(x) dx}, \quad (9)$$

where the assumption has been made that the index ratio $n_o(x)/n_e \approx 1$.

B. Solutions to the Coupled-Mode Equations

By inspection of Maxwell's equations expressed in cylindrical coordinates x , r , and ϕ (see Fig. 1), the electromagnetic field in the plane defined by the radial and azimuthal coordinates is found to be dependent only on the components E_x and H_x . TE modes in the planar waveguide formed by the polymer film are characterized by $E_x = 0$, with the field in the plane of the device thus being entirely characterized by the magnetic component H_x . A standard manipulation then leads to the scalar wave equation

$$\left[\frac{1}{r} \frac{\partial}{\partial r} \left(r \frac{\partial}{\partial r} \right) + \frac{1}{\rho^2} \frac{\partial^2}{\partial \phi^2} + \frac{\partial^2}{\partial x^2} \right] H_x + k_0^2 \epsilon(x, r, \phi) H_x = 0. \quad (10)$$

Solutions to the wave equation can be expanded in a Fourier series to eliminate azimuthal dependence:

$$H_x(r, \phi, x) = \sum_{m=0}^{\infty} H_{xm}(r, x) \exp(im\phi). \quad (11)$$

For a CG-DFB structure centered at the origin of the r , ϕ plane, each Fourier component of the field can be written in the form

$$\begin{aligned} H_{xm}(r, x) = & [A_m(r) H_m^{(1)}(\beta_r \rho) \exp(-i\beta_r r_0) \\ & + B_m(r) H_m^{(2)}(\beta_r \rho) \exp(i\beta_r r_0)] X(x) \\ & + \Delta H_{xm}(r, x), \end{aligned} \quad (12)$$

where $A_m(\rho)$ and $B_m(\rho)$ are the amplitudes of the counterpropagating waves, $H_m^{(1,2)}$ are Hankel functions of the first and second kinds, and β_r is the propagation constant for the guided mode at second-order Bragg resonance. $\Delta H_{xm}(r, x)$ represents the radiated field contribution, in which radiated losses are assumed to be dependent on the field intensity. The phase shift $\exp(\pm i\beta_r r_0)$ represents a change in grating phase at the center of the device that may occur owing to a fabrication defect or from a small unperturbed center section. The center phase shift is conveniently expressed as follows:

$$\Omega = \frac{l\pi}{\Lambda}(\Lambda' + 2r_0), \quad (13)$$

where Λ is the grating period, Λ' is the grating tooth width, and l is an integer denoting the grating order. By use of the large radius approximation for the cylindrical waves, Eq. (12) may be substituted into Eq. (10). A Green's function technique is then utilized to simplify the inclusion of the radiated portion of the general solution:

$$\begin{aligned} \Delta H_{xm}(r, x) = & A_m(r)H_m(1)(\beta_r r)g_1(x)\exp(-i\beta_r r) \\ & + B_m(r)H_m(2)(\beta_r r)g_{-1}(x)\exp(i\beta_r r), \end{aligned} \quad (14)$$

where the coefficients $g_{\pm 1}(x)$ are calculated by integration of the relevant Green's function. It is noted that, except for rapid oscillation terms, the radial dependence of the radiated field is identical to that of the confined field described by the first terms in Eq. (12).

It is convenient for subsequent analysis to define the complex detuning variable:

$$\Delta\beta'_p = \Delta\beta_p + i\Gamma_e\gamma = \left(\beta_r - \frac{p\pi}{\Lambda}\right) + i\Gamma_e\gamma. \quad (15)$$

The real terms in Eq. (15) represent mode detuning from the p th-order Bragg wavelength, and $\Gamma_e\gamma$ is the modal gain.

A perturbation analysis⁵⁻⁷ then follows in which an appropriate refractive-index perturbation is applied to $\epsilon(x, r, \phi)$ in Eq. (10). The following coupled-mode equations are thus derived:

$$\begin{aligned} \frac{d}{dx}A_m(r) = & -(-1)^m i\kappa_f B_m(r) - i\Delta\beta'_2 A_m(r) \\ & - \kappa_r[A_m(r) + (-1)^m B_m(r)], \end{aligned} \quad (16)$$

$$\begin{aligned} \frac{d}{dx}B_m(z) = & -(-1)^m i\kappa_f A_m(r) + i\Delta\beta'_2 B_m(r) \\ & + \kappa_r[(-1)^m A_m(r) + B_m(r)], \end{aligned} \quad (17)$$

with κ_f as the feedback coupling coefficient and κ_r as the radiation coupling coefficient, defined as

$$\kappa_f = \frac{k_o^2 \Delta\epsilon}{2\beta_r V} \int_d |E(x)|^2 C_2(x) dx, \quad (18)$$

$$\kappa_r = \frac{k_o^4 \Delta\epsilon^2}{4\beta_r \beta_x^{(r)} V} \int_d E(x) C_1(x) \exp(j\beta_x^{(r)} x) dx, \quad (19)$$

where k_o is the free-space wave number, given by $2\pi/\lambda$. $\Delta\epsilon$ is the refractive-index step at the grating. $\beta_x^{(r)}$ is the constant of propagation of the radiated field. The integration is performed over d , the depth of the grating; $E(x)$ is the fundamental TE mode profile; and the $C_l(x)$'s, where l is an integer, represent the l th-order Fourier coefficients of the grating index profile. Finally, V is a constant obtained as the integral of the TE mode intensity over all x .

For a grating having a rectangular cross section, the Fourier coefficients are constant throughout the depth of the grating and are written as

$$C_l = \frac{\sin(\pi l \Lambda' / \Lambda)}{\pi l}, \quad (20)$$

where Λ' / Λ is the grating duty cycle. One can analyze symmetric gratings of different profiles by varying the duty cycle throughout the grating depth during the integration in Eqs. (18) and (19).

Equations (16) and (17) are similar to the coupling equations for counterpropagating waves in conventional, linear, second-order DFB lasers. Note, however, that Eqs. (16) and (17) are dependent on the azimuthal mode number m .

C. Analysis of a Circular-Grating Distributed-Feedback Laser at Threshold

A general solution to Eqs. (16) and (17) takes the form

$$A_m(r) = a_f \exp(iqr) + a_b \exp(-iqr), \quad (21)$$

$$B_m(r) = b_f \exp(iqr) + b_b \exp(-iqr), \quad (22)$$

with a_f , a_b , b_f , b_b , and q as values to be sought. Substituting the general solution into the coupling Eqs. (16) and (17), collecting terms of like phase, and evaluating the determinant of the subsequent coefficient matrix results in the following nontrivial solution for eigenvalue q :

$$q(\Delta\beta'_2) = \pm[\Delta\beta'_2{}^2 - k_f^2 + 2j\kappa_r(\kappa_f - \Delta\beta'_2)]^{1/2}. \quad (23)$$

The reflection coefficient between the counterpropagating field components is then calculated as

$$\begin{aligned} R_m(q) = & (-1)^m \frac{-(q + \Delta\beta'_2 - i\kappa_r)}{-i\kappa_r + \kappa_f} \\ = & (-1)^m \frac{-i\kappa_r + \kappa_f}{q - \Delta\beta'_2 + i\kappa_r}, \end{aligned} \quad (24)$$

which allows the general solution to be written as

$$A_m(r) = a_f \exp(iqr) + R_m(q)b_b \exp(-iqr), \quad (25)$$

$$B_m(r) = R_m(q)a_f \exp(iqr) + b_b \exp(-iqr). \quad (26)$$

Equations (25) and (26) can be expressed in a matrix form relating amplitudes $A_m(r)$ and $B_m(r)$ to solution coefficients a_f and b_b for a particular value of r :

$$\begin{aligned} \begin{bmatrix} A_m(r) \\ B_m(r) \end{bmatrix} &= \begin{bmatrix} \exp(iqr) & R \exp(-iqr) \\ R \exp(iqr) & \exp(-iqr) \end{bmatrix} \begin{bmatrix} a_f \\ b_b \end{bmatrix} \\ &= m(r) \begin{bmatrix} a_f \\ b_b \end{bmatrix}. \end{aligned} \quad (27)$$

For a theoretical, annular DFB section between radii $r = R_1$ and $r = R_2$, a transfer matrix, $M(R_1, R_2)$, can be derived thus:

$$\begin{aligned} \begin{bmatrix} A(R_1) \\ B(R_1) \end{bmatrix} &= m(R_1)m(R_2)^{-1} \begin{bmatrix} A(R_2) \\ B(R_2) \end{bmatrix} \\ &= M(R_1, R_2) \begin{bmatrix} A(R_2) \\ B(R_2) \end{bmatrix}, \end{aligned} \quad (28)$$

where $m(R_2)^{-1}$ denotes the left-hand inverse of $m(R_2)$. The transfer matrix relates the counterpropagating amplitude coefficients $A(r)$ and $B(r)$ at the end points of the grating section. A transfer matrix for a grating composed of any number of adjacent elements may be formed by the multiplication of transfer matrices representing the individual elements.

One then obtains the coupled-mode solutions by applying the correct boundary conditions. The boundary conditions for the solutions in the CG-DFB are

$$B_m(R_2) = 0, \quad (29)$$

$$A_m(0) = \exp(i\omega)B_m(0), \quad (30)$$

where R_2 is taken to represent the outer radius of the entire structure and ω is the phase shift seen in the grating at the center point ($r = 0$). The eigenfunction for the lasing modes of the CG-DFB is then

$$\left[\frac{M(r_1, r_2)_{2,1}}{M(r_1, r_2)_{2,2}} + \exp(i\phi) \right] M(r_1, r_2)_{2,2} = 0. \quad (31)$$

The lasing modes are sought as solutions in terms of the complex variable $\Delta\beta'_2$ to Eq. (31). The argument principle method has consistently proved to be a reliable, accurate, and convenient tool for locating solutions to eigenvalue equations of this kind.⁸ Because the modes are not sought as solutions to an explicit eigenfunction, the derivative of the function, required by the argument principle method, is calculated with a Cauchy integration technique rather than analytically.

Following Ref. 9, one obtains a good approximation of the radiated field from the r -dependent intensity envelope of the lasing mode. Once the solutions are found, the transfer matrices M can be used to calculate the values of $A_m(r)$ and $B_m(r)$ throughout the structure. From Eq. (14), applying the large radius approximation and removing rapid oscillations then give the following function for the radially dependent near-field $F(r)$:

$$F(r) = A(r) \left(\frac{2}{i\pi\beta_0 r} \right)^{1/2} i^{-m} + B(r) \left(\frac{2i}{\pi\beta_0 r} \right)^{1/2} i^m. \quad (32)$$

Implementing the transfer-matrix formalism coupled with the argument principle method requires significantly more computing resources than a more analytical technique. However, the execution time rarely exceeds a

few minutes on a typical desktop computer. The advantages of the technique described above stem from its generality. It is possible to analyze both circular and linear structures having multiple sections, and the effects of gain and complex coupling are readily included.

4. ANALYSIS RESULTS

It is assumed that a MEH-PPV film of thickness d_x is deposited onto fused silica (SiO_2). Optical excitation is provided by either a 400- or a 550-nm pump laser. Absorption at the pump wavelength for MEH-PPV is given as $0.25 \times 10^5 \text{ cm}^{-1}$. The refractive index of the substrate is taken as 1.46, and the refractive index of air is assumed to be unity. The air and substrate layers are assumed to have minimal dispersion in comparison with that of the polymer layer, and neither the real nor the imaginary refractive index of MEH-PPV is assumed to vary significantly with pump intensity.

A rectangular profile is chosen for the DFB grating, as this has been shown⁸ to provide superior coupling to other symmetrical grating shapes. The period of the grating is chosen as 400 nm, which matches the second-order Bragg condition for the TE mode.

A. Transverse Waveguide Analysis

It is initially of interest to investigate the optimum planar waveguide geometry for the CG-DFB laser. Specifically, strong pump absorption leading to a nonuniform gain profile is taken into consideration.

For the wavelength range of 580–700 nm, coincident with the emission bandwidth of MEH-PPV, the planar polymer waveguide supports a fundamental TE mode and a fundamental TM mode. Figure 2 shows the intensity profile of the TE mode at 580, 630, and 700 nm. The profile shows good overall confinement to the MEH-PPV region. The fundamental TM profile supported by the waveguide over the wavelength range is shown in Fig. 3. The discontinuity of the field at the interfaces is a characteristic of TM modes. TM mode confinement at 630 nm is much lower than that of the TE mode at the same

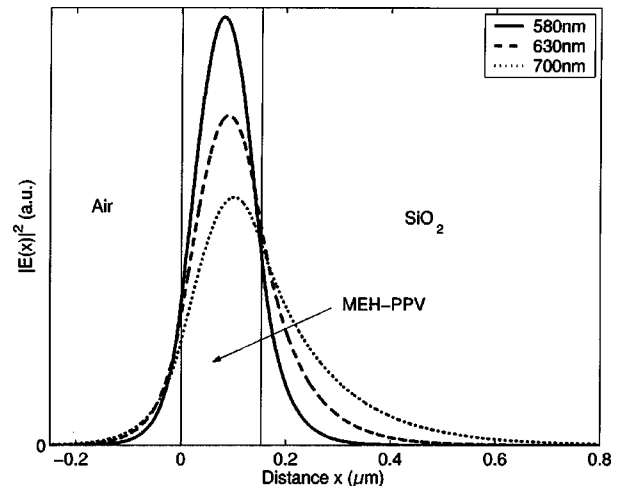


Fig. 2. TE fundamental mode intensity profile at various wavelengths.

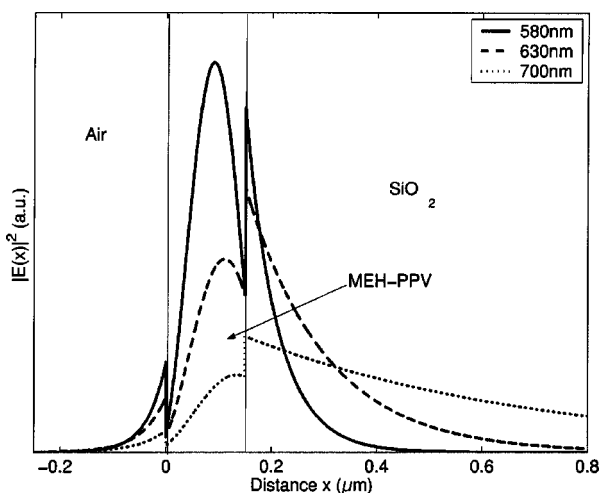


Fig. 3. TM fundamental mode intensity profile at various wavelengths.

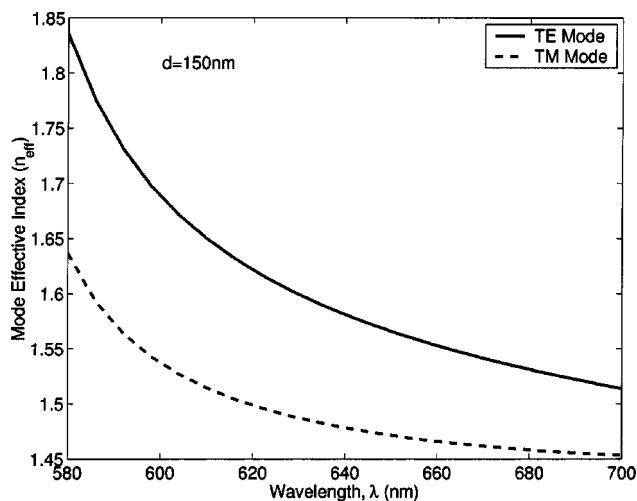


Fig. 4. Dispersion of the MEH-PPV waveguide.

wavelength. Also, it can be seen in Fig. 4 that the dispersion of the TM mode is much greater than for the TE case.

Figure 5 shows the TE confinement defined above. The effective confinement initially improves with increasing MEH-PPV film thickness. As the MEH-PPV layer becomes thicker, however, the mode peak is shifted away from the active area, and the effective confinement is reduced. The optimum film thickness for TE confinement is 140–200 nm. Thickness greater than approximately 240 nm results in a first-order, antisymmetric TE mode that is supported in the waveguide in addition to the symmetric fundamental TE mode.

The TM confinement as a function of film thickness is shown in Fig. 6. Characteristics similar to those calculated for the TE mode can be seen, although TE mode confinement is considerably superior. The optimum film thickness for TM confinement is 200–300 nm.

Planar polymer waveguides fabricated with spin coating typically have thicknesses of 120–150 nm. Because of the much higher confinement of TE modes, they are expected to dominate the oscillating modes of a MEH-PPV laser at or near threshold. As a result, TM modes are not

predicted to be significant near threshold. With this, an experimentally achievable active polymer layer of thickness 150 nm, maximum overlap of the mode with the gain profile is maintained with minimum dispersive loss.

In the subsequent calculations, making the assumption that a single TE mode is present in the planar waveguide leads to a great simplification of the analysis. Given the expected dominance of the fundamental TE mode, it is reasonable to assume that this is the only transverse mode supported by the laser.

B. Coupling Coefficients

By inspection of Eqs. (18) and (19), it is apparent that the calculation of κ_r and κ_f in a polymer-film CG-DFB can be performed without consideration of the circular geometry of the device. The calculation is essentially identical to similar analysis in more usual linear DFB designs.

The duty cycle of the rectangular grating is critical in determining the magnitude of κ_r and κ_f . With d_g denoting the depth of the grating teeth and d_x denoting the thickness of the polymer film, Fig. 7 shows the dependence of the coupling coefficients on the grating duty cycle for a $d_g = 30$ -nm-deep rectangular grating.

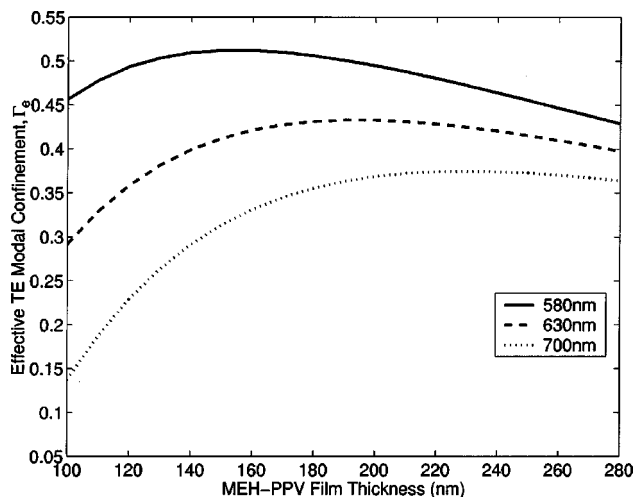


Fig. 5. TE mode confinement versus film thickness.

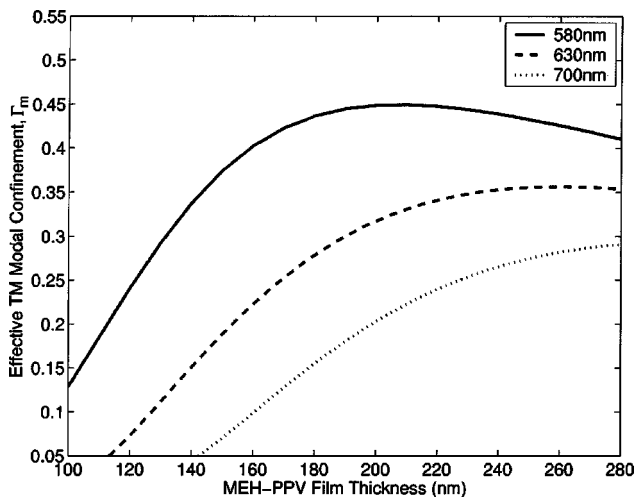


Fig. 6. TM mode confinement versus film thickness.

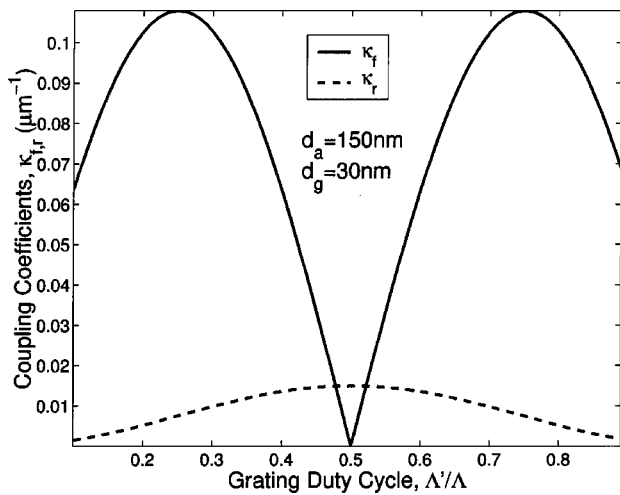


Fig. 7. Effect of the duty cycle on radiation and feedback couplings in a 400-nm-period, 30-nm-depth, second-order, rectangular profile DFB grating.

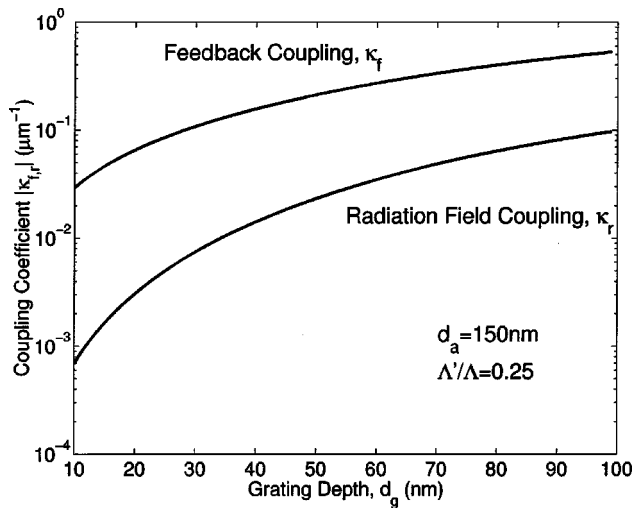


Fig. 8. Radiation and feedback couplings in a 400-nm-period, second-order, rectangular profile DFB grating.

With a duty cycle of one half, κ_f goes to zero, and no feedback coupling occurs because of destructive interference of the counterpropagating optical waves at the Bragg wavelength. Theoretically, this is predicted by the absence of even-order harmonics in the Fourier transform of a rectangular wave and therefore the absence of even-order terms in Eq. (20). A duty cycle of one quarter gives a good compromise between radiation and feedback couplings. Figure 8 shows the dependence of κ_r and κ_f on grating depth for a rectangular grating having a duty cycle of one quarter. It can be seen from the figure that grating thicknesses of around $d_g = 30$ nm provide good feedback and radiation couplings in a one-quarter duty cycle grating.

C. Circular-Grating Distributed-Feedback Operational Characteristics at Threshold

Two CG-DFB designs are proposed to demonstrate the analytical tools described and illustrate how device characteristics may be improved. Design (a) in Fig. 9 is a CG-

DFB having a single 400-nm-period second-order grating extending from $r \approx 0$ to $r = R_2$. Design (b) is a two-section DFB having a 400-nm-period second-order section extending from $r = 0$ to $r = R_1$ and a 200-nm-period first-order section between $r = R_1$ and $r = R_2$. Radiation from the two-section CG-DFB will emerge only from the inner grating section, as no light is coupled out of the device from the first-order outer grating. The pump radiation for both designs is assumed to be uniform across the entire device diameter.

The duty cycle for the single-section CG-DFB design is chosen as one quarter, to provide optimum feedback coupling while maintaining modest coupling to radiation modes. For the two-section CG-DFB, the duty cycle of the second-order inner grating is one quarter, and the first-order outer grating has a duty cycle of one half. This ensures that feedback coupling strength, proportional to the value κ_f , is the same in both gratings, preventing losses arising from feedback coupling at the $r = R_1$ boundary.

Figure 10 shows the first lasing modes of a 100- μ m-diameter single-section polymer CG-DFB on axes of normalized modal gain and detuning. The grating is given a center phase of $\Omega = 2\pi$, corresponding to a continuous

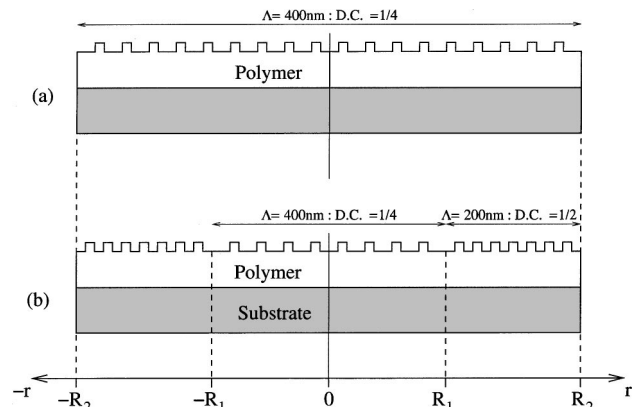


Fig. 9. Design profiles of (a) single-section and (b) two-section polymer CG-DFB lasers. D.C., duty cycle.

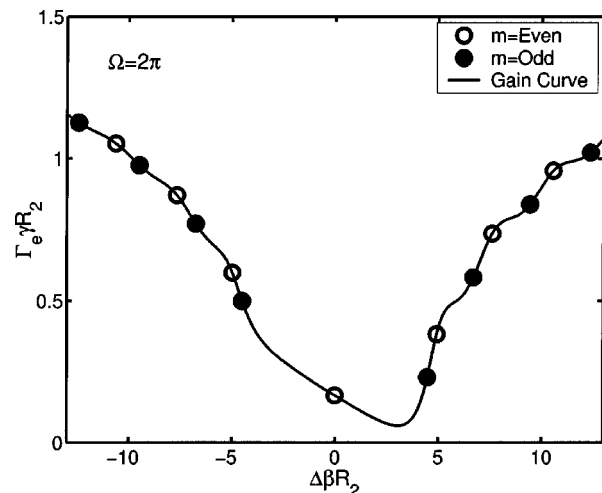


Fig. 10. Lasing modes of a 100- μ m-radius, single-section polymer CG-DFB laser with $\Omega = 2\pi$.

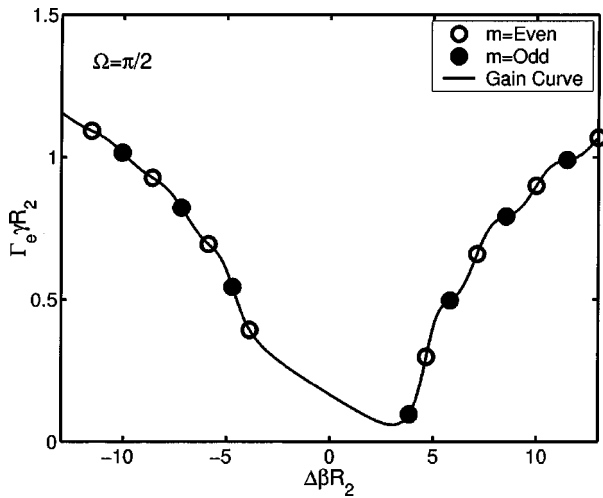


Fig. 11. Lasing modes of a 100- μm -radius, single-section polymer CG-DFB laser with $\Omega = \pi/2$.

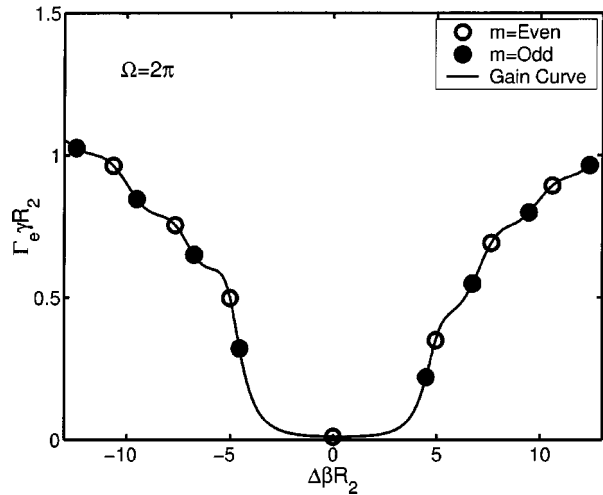


Fig. 12. Lasing modes of a 100- μm -radius, two-section polymer CG-DFB laser with $\Omega = 2\pi$.

grating profile through a cross section of the device. The mode spectra are asymmetric about zero detuning owing to the higher degree of radiation losses at wavelengths lower than the Bragg condition. The modes are found as solutions to Eq. (31), which is dependent on azimuthal mode order m . The solutions are degenerate for even and odd values of m , which has been demonstrated to be a good approximation for azimuthal mode orders in the range $0 < m < 100$.¹⁰ The mode spectra of a similar grating differing only in the center phase value, $\Omega = \pi/2$, are shown in Fig. 11. Comparison between Figs. 10 and 11 reveals that a center phase shift of $\Omega = \pi$ corresponds to an inversion of the roles of the even- and odd-order azimuthal modes. The configuration $\Omega = 2\pi$ gives a single, even azimuthal order, mode at the Bragg wavelength, whereas the $\Omega = \pi/2$ grating offers a lower threshold for the odd azimuthal order mode on the positive band edge. It is preferable to have $m = \text{even}$ azimuthal modes lasing at threshold, as this includes the $m = 0$ azimuthal mode, which has no zero crossings along the angular coordinate. The solid curves shown in

both figures are a result of plotting solutions to Eq. (31) while continuously varying ω between 0 and 2π .

Figure 12 shows the mode spectra of a two-section CG-DFB, with $\Omega = 2\pi$, $R_1 = 50 \mu\text{m}$, and $R_2 = 100 \mu\text{m}$. At higher levels of gain and detuning, the shape of the mode spectra is comparable with that for the single-section design. Near the Bragg wavelength, however, the overall level of threshold is considerably reduced. It is also evident that the reduced radiation loss results in more symmetrical spectra. Again, the effect is most noticeable near the origin of the detuning axis.

Normalized near-field intensities of the first four lowest threshold modes in a single-section CG-DFB are shown in Fig. 13. The increase in intensity toward the center of the device is in agreement with other theoretical results.⁹ It is necessary to plot the log of the field intensity to make the curves of the figure separable for comparison. The near-field intensity curves are numbered in order of increasing threshold of their corresponding modes. Referring to Fig. 10 it can be seen that the lowest threshold mode is an $m = \text{even}$ mode almost exactly at the point of zero detuning. In Fig. 13 it can be seen that the intensity envelope for this mode radiates most power toward the outer rim of the device. Higher threshold modes show more favorable intensity profiles, radiating optical power toward the center.

Figure 14 shows a similar graph for the center section of the $R_1 = 50 \mu\text{m}:R_2 = 100 \mu\text{m}$ two-section device. The mode profiles are similar to those for the single-section device; however, the azimuthal mode orders m of modes (3) and (4) have exchanged as a result of the decrease in radiation loss.

One may obtain far-field approximations by taking the two-dimensional Fourier transform of the near-field intensity profiles. Figure 15 shows the results of this calculation for the single-section DFB modes. The lowest threshold mode has the most favorable characteristic, with the emission being focused in a single, narrow lobe. Higher threshold modes are seen to emit at an angle of around 0.2 deg from normal incidence. As can be seen in Fig. 16, the use of a two-section device makes the modes

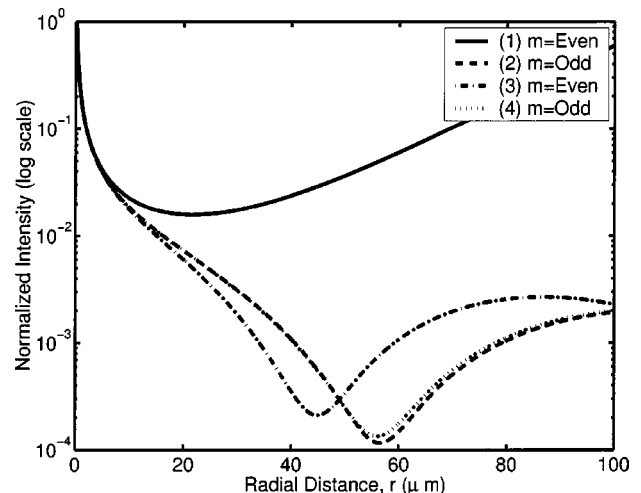


Fig. 13. Near-field intensity of the first four lasing modes in a 100- μm -radius, single-section polymer CG-DFB laser with $\Omega = 2\pi$.

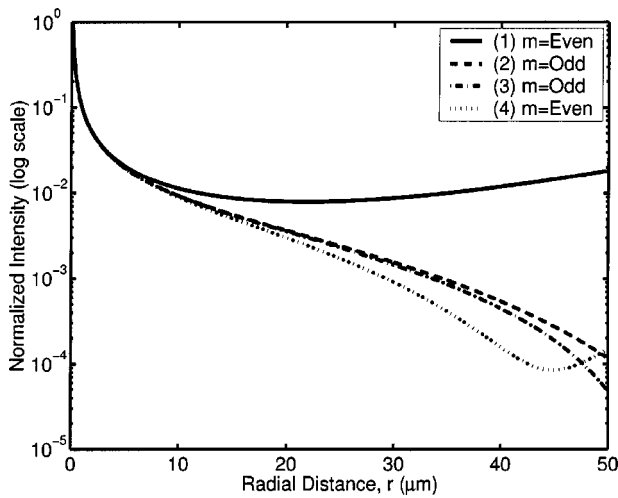


Fig. 14. Near-field intensity of the first four lasing modes in a 100- μm -radius, single-section polymer CG-DFB laser with $\Omega = 2\pi$.

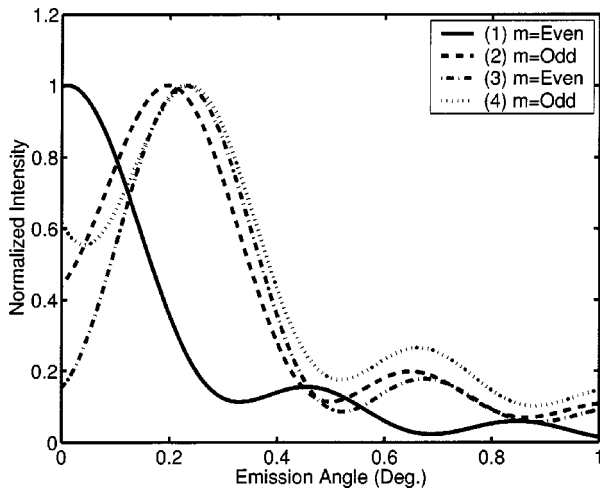


Fig. 15. Far-field intensity of the first four lasing modes in a 100- μm -radius, single-section polymer CG-DFB laser with $\Omega = 2\pi$.

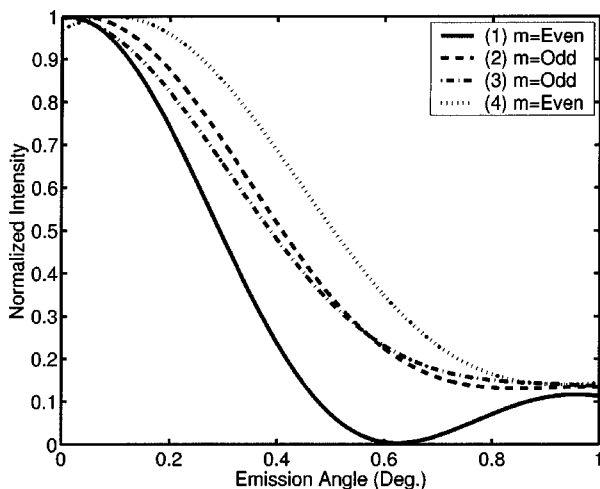


Fig. 16. Far-field intensity of the first four lasing modes in a 100- μm -radius, two-section polymer CG-DFB laser with $\Omega = 2\pi$.

emission characteristics much more uniform, with at least the first three lowest threshold modes' output occurring along the axis of normal incidence.

5. CONCLUSION

It has been demonstrated how the transverse TE and TM optical waveguide modes supported by a MEH-PPV polymer film on a silicate substrate may be calculated. Use of an experimentally derived Sellmeier function for the refractive index of MEH-PPV permits the dispersion in the polymer waveguide to be studied. In calculations involving optically pumped laser devices, the high absorption of radiation at the pump wavelength results in a strongly nonuniform gain profile that reduces the optimal film thickness for use in the laser waveguide. Assuming an operating wavelength of around 630 nm, near the emission peak for MEH-PPV polymer, an optimum film thickness of 150 nm supports a fundamental TE mode having a maximum effective confinement of $\Gamma_e = 0.4$. Although a fundamental TM mode is also supported in this waveguide geometry, the confinement of this mode is not sufficient ($\Gamma_e = 0.1$) for it to be considered in addition to the well-confined TE mode.

With information on the optical confinement and mode profile of the supported TE mode, the lasing modes of two vertically emitting circular-grating DFB (CG-DFB) structures have been investigated. One structure features a single-section second-order CG-DFB grating that gives coupling to emission across the entire diameter of the laser, and the other is a two-section design featuring a smaller second-order grating combined with a first-order grating that provides feedback only.

The lasing mode spectra of both structures show the asymmetrical effects of loss due to radiation via the second-order grating components. For the two-section design, the symmetry of the mode spectra is partially restored near the Bragg wavelength as a result of the reduced amount of loss from the much smaller area of emission. Although the phase of the grating at the center can be adjusted to change mode selection, it is known that having no phase change across the center ($\Omega = 2\pi$) results in a single mode oscillating near the Bragg wavelength with low threshold. In CG-DFB lasers featuring strong radiation loss, however, a phase shift of $\Omega = \pi/2$ gives the lowest possible threshold for lasing, albeit on the positive edge of a stop band formed around the Bragg wavelength.

The lowest threshold mode of the CG-DFB with $\Omega = 2\pi$ has an intensity profile that increases toward the edge of the device. Higher-order modes offer more favorable near-field profiles at the cost of higher threshold and radiation lobes away from normal incidence when the far field is calculated. Using the two-section design is shown to offer more favorable emission characteristics for the modes near threshold as well as reducing threshold gain for the mode oscillating at the Bragg frequency.

The results of the threshold gain analysis in MEH-PPV CG-DFB lasers show a strong qualitative resemblance to similar studies of CG-DFB lasers in inorganic systems,⁹⁻¹¹ in which the radial modes of the CG-DFB were analyzed with an explicit dispersion function. The

transfer-matrix approach presented here has been shown to reproduce the results of Refs. 9–11 exactly when data sets identical to those found in the literature are supplied. In addition, the methods outlined in the present paper may be adapted for the analysis of circularly symmetric DFB structures containing any number of concentrically arranged components without the need to derive a specific dispersion function for each design.

The polymeric laser designs under analysis generally exhibit lower gain thresholds owing to much stronger coupling arising from the high optical confinement of the TE mode. This is in accordance with previous studies of waveguiding in optical organic waveguides⁴ in which high optical confinement and low propagation losses were noted.

It is well known that the perturbation technique described above is best suited to DFB structures on waveguides having a low refractive-index contrast between the guiding layer and the cladding. The assumption that the form of the optical field profile remains constant along the length of the feedback region, made in the derivation of Eqs. (16) and (17), may possibly become less appropriate in waveguides having a large index step.

It is noted that just such a high refractive-index contrast exists in the PPV waveguide at the air–polymer interface. However, the high confinement of the single TE mode, together with the shallow modulation depth of the gratings under analysis, suggests the accuracy of the technique in the specific cases described may still be reasonable. Reference is made to Fig. 5, where it can be seen that the confinement of the TE mode to the active area will be particularly insensitive to small perturbations of the waveguide thickness for optimum PPV film thicknesses of 150–200 nm. It is therefore likely that the optical field profile of the TE mode will be largely unaffected by the index perturbation of the grating. Further investigations into the accuracy of the perturbation theory in polymer DFB waveguides compared with precise computational numerical methods is a matter for future research.

The previous discussion has illustrated how calculations concerning the design of MEH-PPV polymer CG-DFB lasers have been undertaken. It has also been

shown how the use of novel grating designs that exploit new methods of fabricating DFBs on polymer films can be used to control the emission and threshold characteristics of such a laser.

G. F. Barlow, the corresponding author, can be reached by e-mail at guy@sees.bangor.ac.uk.

REFERENCES

1. V. G. Kozlov, G. Parthasarathy, P. E. Burrows, V. B. Khalfin, J. Wang, S. Y. Chou, and S. R. Forrest, "Structures for organic diode lasers and optical properties of organic semiconductors under intense optical and electrical excitations," *IEEE J. Quantum Electron.* **36**, 2596–2606 (2000).
2. M. D. McGhehee, M. A. Diaz-Garcia, F. Hide, R. Gupta, E. K. Miller, and D. Moses, "Semiconducting polymer distributed feedback lasers," *Appl. Phys. Lett.* **72**, 1536–1538 (1998).
3. M. Berggren, A. Dodabalapur, R. E. Slusher, A. Timko, and O. Nalamasu, "Organic solid-state lasers with imprinted gratings on plastic substrates," *Appl. Phys. Lett.* **72**, 410–411 (1998).
4. G. F. Barlow and K. A. Shore, "Analysis of waveguide properties of organic semiconductor lasers," *IEE Proc.: Optoelectron.* **146**, 15–20 (1999).
5. C. Wu, T. Makino, J. Glinski, R. Maciejko, and S. I. Najafi, "Self-consistent coupled-wave theory for circular gratings on planar dielectric waveguides," *J. Lightwave Technol.* **9**, 1264–1277 (1991).
6. C. Wu, T. Makino, R. Maciejko, and S. I. Najafi, "Simplified coupled-wave equations for cylindrical waves in circular grating planar waveguides," *J. Lightwave Technol.* **10**, 1575–1589 (1992).
7. C. Wu, T. Makino, R. Maciejko, S. I. Najafi, M. Svilans, J. Glinski, and M. Fallahi, "Threshold gain and threshold current analysis of circular grating DFB and DBR lasers," *IEEE J. Quantum Electron.* **29**, 2596–2606 (1993).
8. G. F. Barlow and K. A. Shore, "Application of the argument principle method to the calculation of DFB laser diode modes," *Int. J. Numer. Model.* **14**, 291–302 (2001).
9. P. L. Greene and D. G. Hall, "Effects of radiation on circular-grating DFB lasers. I. Coupled-mode equations," *IEEE J. Quantum Electron.* **37**, 353–364 (2001).
10. A. M. Shams-Zadeh-Amiri, X. Li, and W. P. Huang, "Above threshold analysis of second-order circular-grating DFB lasers," *IEEE J. Quantum Electron.* **36**, 256–267 (2000).
11. T. Erdogan and D. G. Hall, "Circularly symmetric distributed feedback semiconductor laser: an analysis," *J. Appl. Phys.* **68**, 1435–1444 (1990).